J. Fluid Mech. (2002), *vol.* 460, *pp.* 131–149.
DOI: 10.1017/S002211200200808X Printed in the United Kingdom

Onset of menisci

By CHRISTOPHE CLANET[1] AND DAVID QUÉRÉ[2]

[1]Institut de Recherche sur les Phénomènes Hors Equilibre,
UMR 6594, 49 rue F. Joliot Curie, B.P. 146, 13384 Marseille, France

[2]Laboratoire de Physique de la Matière Condensée, URA 792 du CNRS, Collège de France,
75231 Paris Cedex 05, France

(Received 24 July 2001 and in revised form 8 November 2001)

When a vertical solid is brought in contact with the surface of a wetting liquid, a meniscus starts rising up the solid, until it reaches its steady state. We study this dynamical phenomenon experimentally with liquids of low and high viscosity, and taking as solids either large rods or small fibres. In the inviscid limit, we show that the rising time scales as $\sqrt{\rho r_0^3/\sigma}$, where ρ and σ are the density and surface tension of the wetting liquid and r_0 the radius of the fibre. This characteristic time holds for small fibres, with radii smaller than the capillary length a. For large rods or planar solids, r_0 is replaced by a in the expression for the rising time. In the viscous limit, the rising time scales as $\eta r_0/\sigma$ where η is the dynamical viscosity. Again, r_0 is replaced by the capillary length a for large rods.

1. Introduction

In ancient Greek, 'mênê' designated the moon. It became the root of the word 'meniscus' which stands for a crescent of the moon and is associated with the wetting of a liquid on a solid. An example of liquid meniscus is presented in figure 1(*b*): a vertical planar wall initially held above a horizontal interface (figure 1*a*) is lowered to contact with a wetting liquid (contact angle θ_e smaller than $\pi/2$), which forces the liquid to develop a meniscus of typical size l.

The liquid being characterized by its density ρ and surface tension σ, the shape of the interface results from the equilibrium between the Laplace depression, of order σ/l, and the gravitational depression of order $\rho g l$, where g is the acceleration due to gravity. The balance between these two terms leads to $l \sim a$, where $a \equiv \sqrt{\sigma/\rho g}$ is the capillary length of the interface. In the case of a water/air interface on Earth, $\sigma \approx 0.073\,\mathrm{kg\,s^{-2}}$, $\rho \approx 10^3\,\mathrm{kg\,m^{-3}}$, $g \approx 9.81\,\mathrm{m\,s^{-2}}$ so that $a \approx 2.7\,\mathrm{mm}$. This shape remains unchanged as long as the radius of the wall r_0 is larger than a ($r_0 = \infty$ for a planar wall). In the limit $r_0 \ll a$, the pressure balance is dominated by the Laplace pressure associated with the two radii of curvature of the interface, and gravity can be neglected in the region close to the fibre. In this limit, l becomes of the order of r_0, as it can be observed in figure 1(*c*), where r_0/a is 0.08. The same scaling is found for menisci in capillary tubes, since these menisci are (almost) spherical for $r_0 \ll a$, r_0 being here the internal tube radius.

Historically, the physical origin and the shape of the static meniscus have been among the first phenomena studied in capillarity, in particular by Hauksbee (1709), as cited by Maxwell (1875) in his introduction to the *Capillary Action* written for the *Encyclopaedia Britannica*: "the first accurate observations of the capillary action of

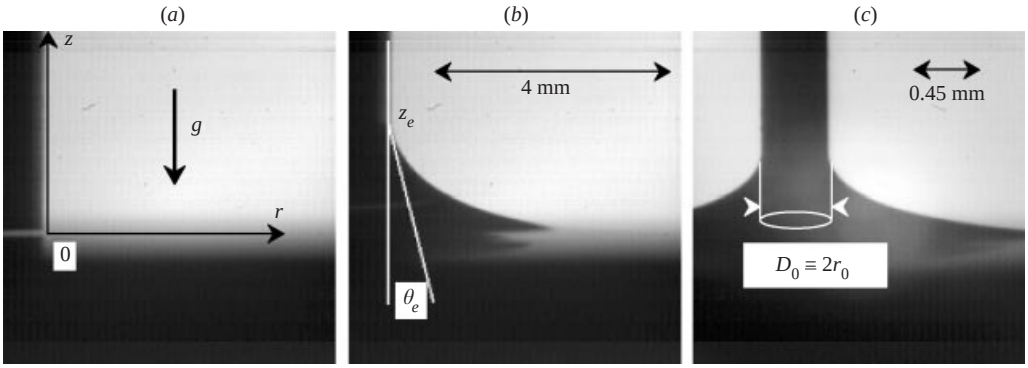

FIGURE 1. Example of static menisci observed with a wetting liquid (hexane): (*a*) planar wall just before the contact, (*b*) meniscus on a planar wall a 'long' time after the contact, (*c*) meniscus on a fibre of diameter $r_0 = 0.225$ mm a 'long' time after the contact.

tubes and glass plates were made by Hauksbee. He ascribes the action to an attraction between the glass and the liquid".

The first theoretical solution of the shape of the static meniscus on a planar wall is due to Laplace (1806). In this configuration, the Laplace equation $\sigma C = \rho g z$, where C is the curvature of the interface, can be integrated twice with appropriate boundary conditions. This classical analytical solution is presented in Bouasse (1924) and can also be found in Landau & Lifchitz (1971). In the limit $r_0/a \ll 1$, there is no general analytical solution and the problem of the static meniscus shape has been addressed numerically by White & Tallmadge (1965). Analytically, the shape can be approached as follows: in the region close to the fibre, the Laplace equation is reduced to $\sigma C = 0$, which can be integrated in axisymmetric coordinates. This provides a catenary as a shape for the interface. This catenary can only match the reservoir if gravity is taken into account, with an appropriate asymptotic matching technique, first developed by James (1974) and improved by Lo (1983). The stability of these static solutions has been discussed by Pitts (1976).

We are interested in this article in determining the dynamics of the meniscus from the contact ($t = 0$) to the static regime ($t = \infty$), for different fibre radii r_0 and various liquid viscosities η. Applications are numerous, from surface tension measurement devices to welding and soldering processes, via surface coating methods. This problem has been discussed in the case of a meniscus rising inside a capillary tube. In the viscous regime described by Washburn (1921), balancing viscosity with capillary force leads to a diffusive-type law ($z \sim \sqrt{t}$, z being the height of the meniscus). Then, gravity slows down the process and causes the height to relax exponentially towards its equilibrium value. The inertial regimes (which are particularly relevant at short time) were discussed more recently: balancing inertia with the capillary force leads to a constant velocity of rise ($z \sim t$), possibly followed by a parabolic saturation due to gravity and oscillations damped against time (Quéré 1997).

Here, unlike the tube case, the geometry is open, which makes both the height of the rise and the shape of the meniscus unknown. This class of problem was first discussed by Keller & Miksis (1983) in the inviscid limit and for large Bond numbers ($Bo \equiv r_0/a$). In this case, they found a self-similar solution in which the meniscus height z varies as $(t^2\sigma/\rho)^{1/3}$. The characteristic time for the meniscus onset, t_e, can thus be evaluated: for $z \sim a$, we find $t_e \sim (\sigma/(\rho g^3))^{1/4}$. This analysis holds provided that the Reynolds number $Re \approx z(\mathrm{d}z/\mathrm{d}t)/\nu$ remains large compared to 1, with $\nu \equiv \eta/\rho$ the

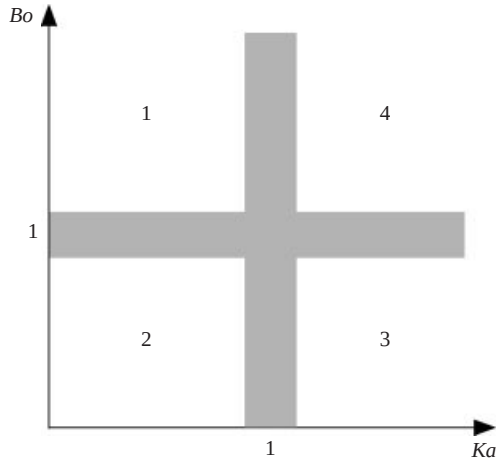

FIGURE 2. Parameter space (Ka, Bo) and definition of the different domains to be investigated. The Kapitsa number is fixed by the liquid properties, and the Bond number by the solid geometry.

kinematic viscosity. Using the previous scalings, this condition corresponds to large Kapitsa numbers ($Ka = [\sigma^3/(\rho^3 g v^4)]^{1/4}$)†. In the (Ka, Bo) parameter space presented in figure 2, the region investigated by Keller & Miksis is domain 4.

Menisci of viscous liquids along small fibres (domain 2) have been studied experimentally by Quéré & di Meglio (1994). Using a quasi-steady approach and Tanner's law for the dynamic contact angle (Tanner 1979), they show that the characteristic time associated with the rise scales as $\eta r_0/\sigma$. This time increases with the fibre radius, but should saturate at a value of order $\eta a/\sigma$, in the limit of large fibres ($Bo \gg 1$). These authors did not visualize the interface directly but only measured the variation of the dynamic contact angle as it approaches equilibrium.

In § 2, we present the experimental apparatus used to observe and quantify the dynamics of menisci. The experimental results are displayed in § 3, prior to the models in § 4 and the conclusions in § 5.

2. Experimental set-up

The experimental apparatus is sketched in figure 3. A cylindrical rod is hung above the liquid interface and its height adjusted via a micro-control translation table. To avoid oscillations of the rod when approaching the interface, we used a contact-free damping device which does not alter the verticality but increases the friction with the surrounding air. This setup ensures that the rod is perpendicular to the interface. The rise of the meniscus was observed with a high-speed video camera Kodak-HS-4540 coupled with a zoom and a micro-computer, using a backlight scattering method. To avoid reflection and refraction problems across the containing glass walls, the reservoir was slightly overfilled.

As shown in figure 1(a), the spatial origin can be precisely determined using the reflection on the liquid surface. The spatial resolution depends both on the size of the CCD matrix (256×256) and on the magnification of the zoom which was adjusted so that the final meniscus height z_e occupied the full screen. The spatial resolution

† This non-dimensional number is often called the Morton number, following Haberman & Morton (1954). However, as mention in Fulford (1964), Kapitsa (1948) introduced the same dimensionless quantity in his study on the flow of thin films.

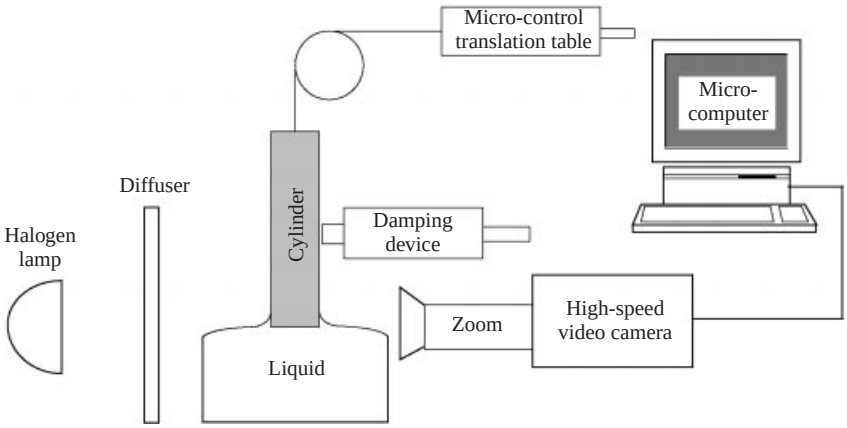

FIGURE 3. Presentation of the experimental set-up.

Fluid	$\rho\,(\mathrm{kg\,m^{-3}})$	$\nu\,(\mathrm{mm^2\,s^{-1}})$	$\sigma\,(\mathrm{kg\,s^{-2}})$	$Ka \equiv \left(\frac{\sigma^3}{\rho^3 g \nu^4}\right)^{1/4}$	$a \equiv \sqrt{\sigma/\rho g}\,(\mathrm{mm})$
Hexane	660	0.45	0.018	481	1.7
V1	815	1.0	0.021	204	1.6
V5	913	5.0	0.021	37	1.5
V10	930	10	0.021	18	1.5
V100	952	100	0.021	1.82	1.5
V1000	962	1000	0.021	0.18	1.5
V12500	965	12500	0.021	0.01	1.5
Water	1000	1.0	0.073	446	2.7

TABLE 1. Physical properties of the different liquids used at room temperature, 22 °C. The V series correspond to silicone oils.

$r_0\,(\mathrm{mm})$	0.0625	0.13	0.225	0.5	1.0	2.0	4.0	8.0
Bo	0.04	0.08	0.15	0.33	0.66	1.33	2.66	5.33

TABLE 2. Radii r_0 of the cylinders and corresponding Bond numbers (taking $a = 1.5\,\mathrm{mm}$).

can thus be evaluated to $z_e/256$ by pixel and the precision on the interface location to ± 3 pixels.

The reflection also allows us to determine precisely the contact time $t = 0$. The uncertainty we have on the time scale is the interval between two images. It thus depends directly on the recording rate, which could be varied from 30 pictures per second (p.p.s.) to 18 000 p.p.s. according to the liquid viscosity.

We used as liquids silicone oils (Polydimethylsiloxane) and hexane, of kinematic viscosities ranging between 0.45 and $12\,500\,\mathrm{mm^2\,s^{-1}}$. Their properties are given in table 1. As well as the density, viscosity and surface tension, we also display in table 1 the Kapitsa number and the capillary length. The corresponding values for water are indicated for comparison.

Finally, the solids were either stainless steel rods or thin tungsten wires. Their characteristic radii, r_0, are displayed in table 2, together with typical values of Bond numbers (taking $a = 1.5\,\mathrm{mm}$).

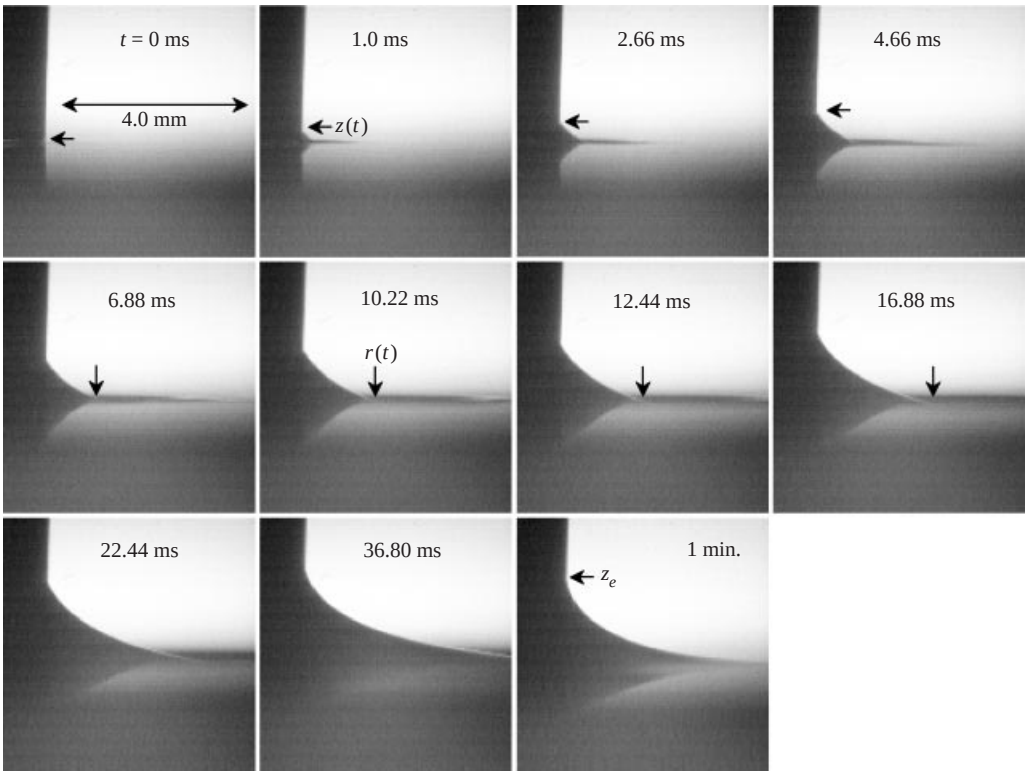

FIGURE 4. Example of meniscus dynamics obtained with hexane and $r_0 = 8.0\,\text{mm}$ (4500 p.p.s.). Each picture corresponds to an evolution $z(t)/z_e = i/10$, where $i \in [0, 10]$ is an integer.

3. Experimental results

We present in figure 4 a series of pictures showing the onset of a meniscus for hexane and $r_0 = 8\,\text{mm}$. The spatial scale is indicated in the top left image and the time written in each picture. Time increases from left to right and from top to bottom. The observed parameters $z(t)$ and $r(t)$ are indicated with arrows on the first and second line, respectively. The last image is taken after 1 min. and corresponds to the equilibrium ($z_e \approx 2\,\text{mm}$). The whole sequence presents the phenomenon at $z(t)/z_e = \{0, 0.1, 0.2, 0.3, 0.4, 0.5, 0.6, 0.7, 0.8, 0.9, 1\}$.

The first indicator we have chosen to characterize the dynamics of the meniscus is the time t_z needed to reach a given location z. This time is used to quantify the effect of the liquid viscosity. For $z = 0.25z_e$, $0.5z_e$ and $0.8z_e$, figure 5 shows the evolution of t_z with the viscosity, for $r_0 = 8.0\,\text{mm}$.

For a given z, t_z remains constant at small viscosities and increases almost linearly with v at large viscosities. The transition between the viscous-dependent and the viscous-independent domains occurs around $v = 10\,\text{mm}^2\,\text{s}^{-1}$, which corresponds to a Kapitsa number of order 10. The transition region does not depend on z. As t_z increases with z, the general features of the evolution are conserved and the transition always occurs in the same range of viscosity.

Taking $v = 0.45\,\text{mm}^2\,\text{s}^{-1}$ to represent the inviscid domain, we show in figure 6(a) the influence of the fibre radius r_0 on the time t_z, for $z = 0.2$ and $0.4\,\text{mm}$. It is observed that for a radius r_0 larger than 0.5 or 1 mm, the time t_z needed to reach $z = 0.2\,\text{mm}$ is the same ($t_z \approx 1\,\text{ms}$). For radii smaller than 0.5 mm, t_z increases as the

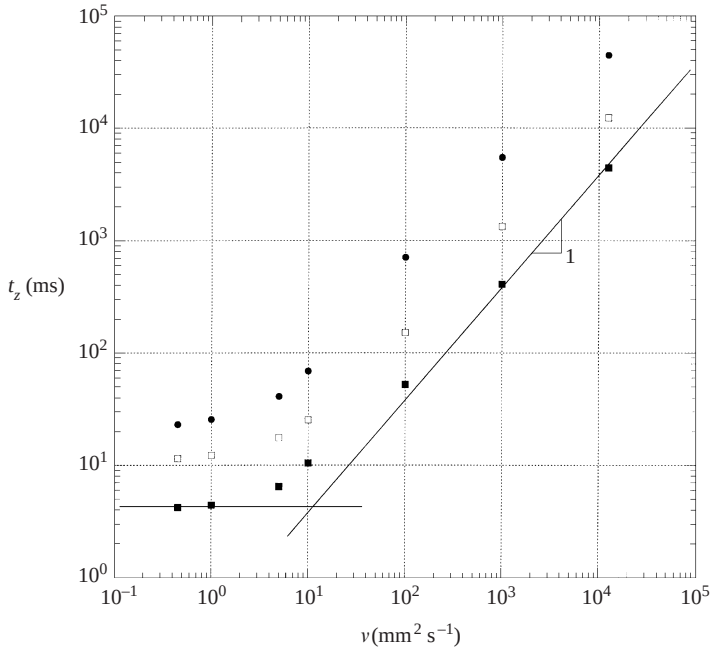

FIGURE 5. Evolution of the indicator time t_z with the viscosity, for different values of z: ■, $z = 0.25z_e$; □, $z = 0.5z_e$; ●, $z = 0.8z_e$.

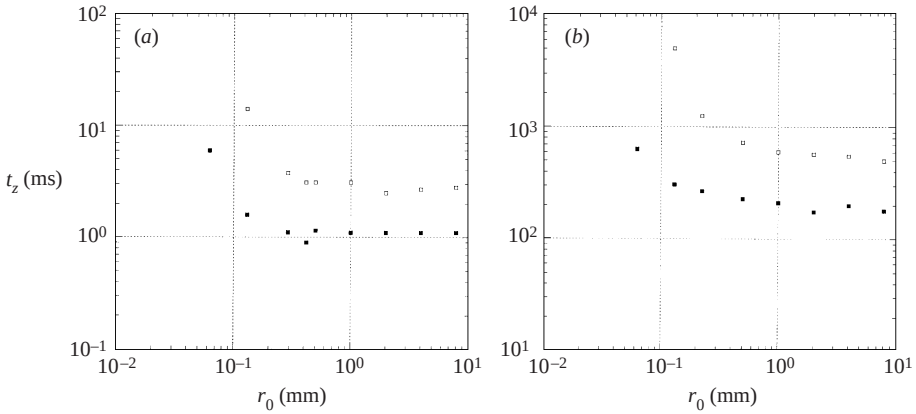

FIGURE 6. Evolution of the indicator time t_z with the fibre diameter r_0, in the inviscid domain (a) and in the viscous domain (b): ■, $z = 0.2$ mm; □, $z = 0.4$ mm.

radius is decreased. It takes for example 6 ms to reach $z = 0.2$ mm for $r_0 = 0.0625$ mm. One could say that for this scaled height, the smaller the fibre the slower the rise (which physically shows the opposing role of the second curvature, associated with the fibre radius, and which generates a positive Laplace pressure). The evolution is similar with $z = 0.4$ mm, where the transition also occurs between 0.5 and 1 mm, which corresponds to a Bond number of order 1.

Using the same indicator, figure 6(b) shows the evolution of $t_z(r_0)$ observed in the viscous domain with $v = 1000\,\text{mm}^2\,\text{s}^{-1}$. For radii larger than 0.5 or 1 mm, the time t_z required to reach $z = 0.2$ mm remains constant ($t_z \approx 200$ ms). Again, for smaller radii, t_z increases as r_0 is decreased. These behaviours are the same for $z = 0.4$ mm.

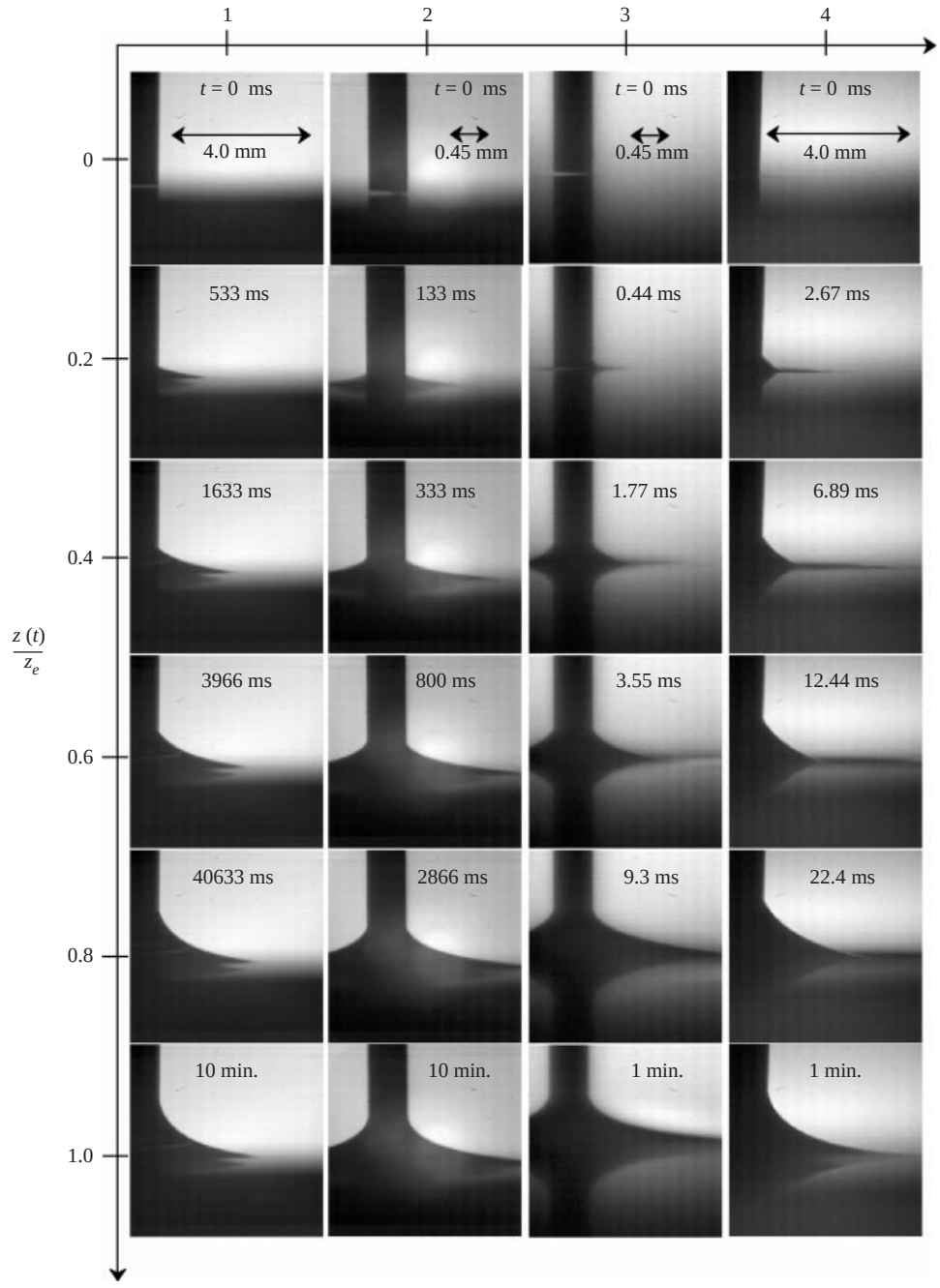

FIGURE 7. Presentation of the dynamics of the interface from $z/z_e = 0$ to $z/z_e = 1$ for the four different domains identified in figure 2.

Hence, figures 5 and 6 allow us to make precise the boundaries of the different domains displayed in figure 2. For each domain, we present in figure 7 an example of the meniscus shape. In each case, the meniscus is shown at six different z/z_e locations: 0, 0.2, 0.4, 0.6, 0.8 and 1, for which the corresponding times are indicated.

In the inviscid domains 3 and 4, in the range $z/z_e \leqslant 1/2$, the radial and the vertical

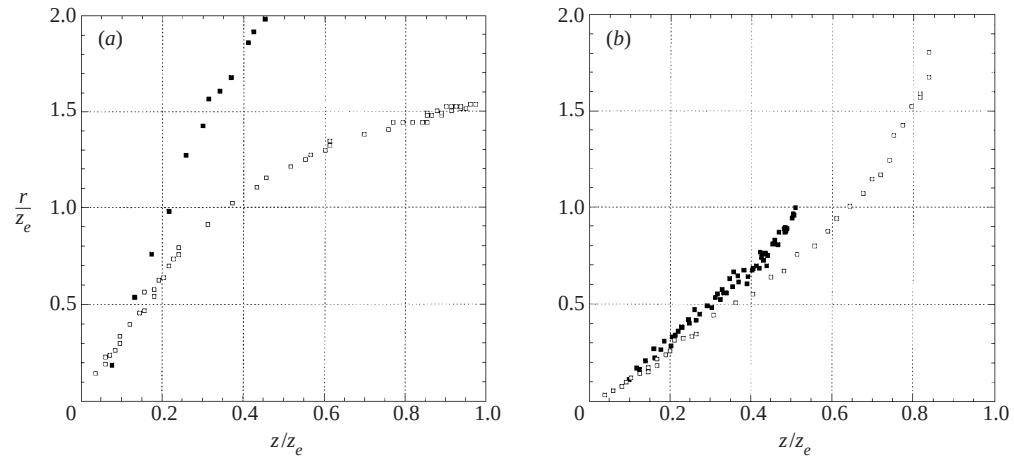

FIGURE 8. Evolution of the radial extent $r(t)/z_e$ as a function of the meniscus height $z(t)/z_e$, for different fibre radii: ■, $r_0 = 0.225$ mm; □, $r_0 = 4$ mm; and different liquids: (*a*) V1000, (*b*) hexane.

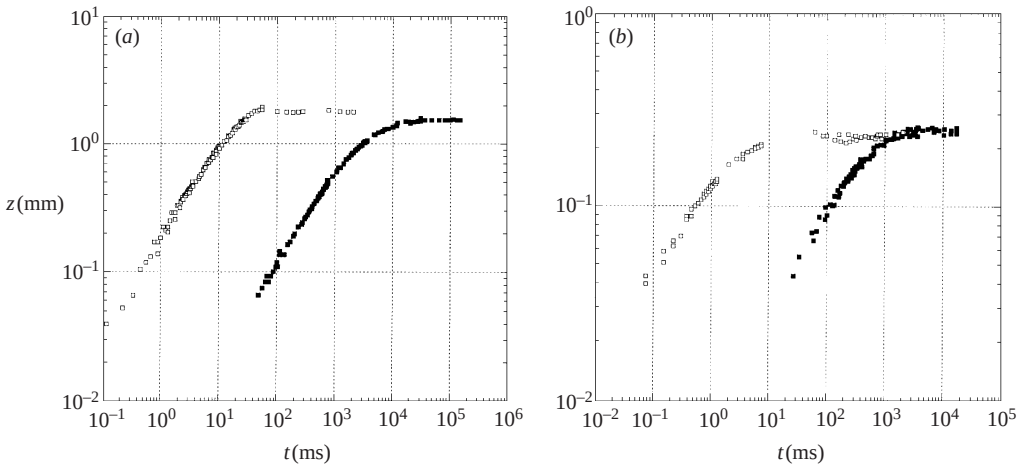

FIGURE 9. Influence of the viscosity on the dynamics of the contact line with (*a*) non-curved meniscus obtained with $r_0 = 4.0$ mm (■, domain 1 obtained with V1000; □, domain 4 obtained with hexane), (*b*) curved meniscus obtained with $r_0 = 0.0625$ mm (■, domain 2 obtained with V1000; □, domain 3 obtained with hexane).

extents seem to develop on a similar time scale. Looking at the junction between the meniscus and the horizontal level, one observes that the interface is perturbated ahead of the meniscus showing the existence of a 'depression' wave.

In the viscous domains 1 and 2, no waves are visible ahead of the meniscus, and the meniscus spreads faster radially than vertically.

As can be expected, the final meniscus shape is the same for a given Bond number, whatever the viscosity of the liquid, provided that the static contact angle is the same. This can be observed in figure 7, where domains 1 and 4 appear to have a similar final state, as do domains 2 and 3.

Focusing on the apparent conical shape of the meniscus at short times, we present in figure 8 the radial extent $r(t)/z_e$ as a function of the height evolution $z(t)/z_e$, for both V1000 (figure 8*a*) and hexane (figure 8*b*).

In the range $z(t)/z_e \ll 1$, it is observed that the vertical and the radial extents can be related by a linear relation $r \approx \alpha z$. For V1000, this behaviour holds up to $z \approx 0.3 z_e$ and α is of order 3 for the large rod and of order 5 for the small fibre. For hexane, the linear behaviour extends further, up to $z \leqslant 0.6 z_e$ and α is of order 1.4 and 1.7 respectively for the rod and for the fibre.

Concerning the dynamics of the rise, we present in figure 9 the influence of the viscosity on the position of the contact line z. The large Bond number limit is obtained with $r_0 = 4.0$ mm. The dynamics observed in domain 1 with V1000 and in domain 4 with hexane is displayed in figure 9(a). Both trajectories tend to the same asymptotic value $z_e \approx 2$ mm, with two characteristic times, $t_e \approx 50$ ms for hexane and $t_e \approx 10\,000$ ms for V1000. The steady state is reached after a growth phase which is not very different for the two liquids and which looks like a power law in time, $z \sim t^{0.7}$. The transition towards the steady state is smoother in the viscous case.

Similarly, figure 9(b) presents the trajectories observed with the same fluids in the small Bond number limit ($r_0 = 0.0625$ mm). The asymptotic limit $z_e \approx 0.26$ mm is reached after a characteristic time $t_e \approx 20$ ms with hexane and $t_e \approx 3000$ ms with V1000. Again, the dynamical phase looks similar in the viscous and inviscid cases, but the scaling is found to be different: $z \sim t^{0.5}$.

4. Models

This section is devoted to a presentation and an analysis of models. We successively discuss the statics, and the dynamics of the rise.

4.1. *Static meniscus*

4.1.1. *The general equation of the shape*

The equation of the static meniscus is obtained by balancing at each point of the interface the hydrostatic pressure $P_a - \rho g z$ with the Laplace pressure $P_a + \sigma C$, where P_a is the ambient pressure and C the curvature of the interface at the curvilinear coordinate s (Bouasse 1924). With the conventions presented in figure 1, $s = 0$ at the wall, where $r = 0$ and $z = z_e$.

This pressure balance leads to the following equation for the meniscus shape:

$$\frac{\mathrm{d}\theta}{\mathrm{d}s} - \frac{\cos\theta}{r + r_0} = \frac{z}{a^2}, \tag{4.1}$$

where we have used the expression for the curvature $C = -\mathrm{d}\theta/\mathrm{d}s + \cos\theta/(r + r_0)$. Equation (4.1) must be integrated with the conditions $\theta(r = 0) = \theta_e$ and $\theta(z = 0) = \pi/2$. Whatever the fibre radius r_0, equation (4.1) admits a first integral which allows us to determine the volume of liquid V above the reservoir level $z = 0$:

$$V = 2\pi r_0 a^2 \cos\theta_e. \tag{4.2}$$

4.1.2. *Meniscus on a planar wall*

The meniscus on a planar wall corresponds to the limit $r_0 \gg a$. Then, equation (4.1) reduces to $\mathrm{d}\theta/\mathrm{d}s = z/a^2$. The first integration of this reduced form gives the relation $z(\theta)$:

$$z = \sqrt{2(1 - \sin\theta)}\, a. \tag{4.3}$$

For $\theta = \theta_e$ we find that the meniscus height is $z_e = \sqrt{2(1 - \sin\theta_e)}\, a$, which can thus vary from 0 to $2a$. In the case $\theta_e = 0$, we observe that $z_e = \sqrt{2}a$.

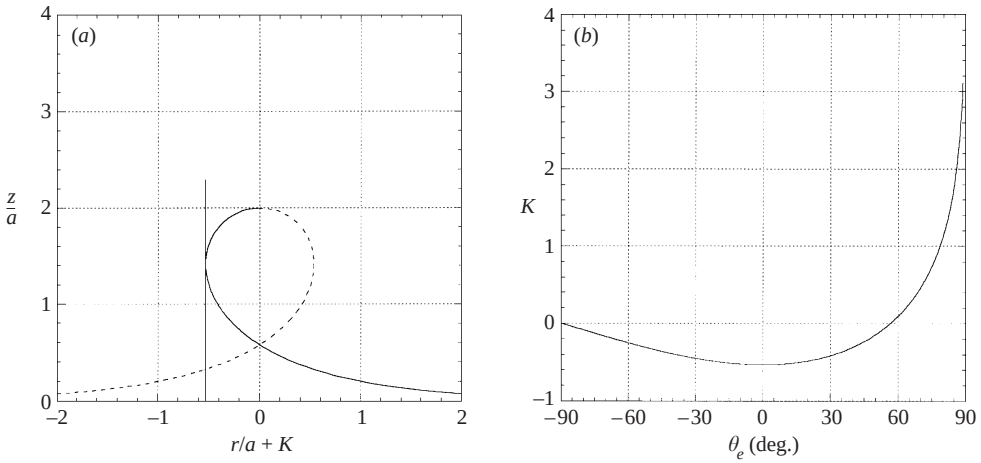

FIGURE 10. Static meniscus on a wall: (*a*) the general shape $z/a(r/a+K)$. (*b*) Determination of the constant K as a function of θ_e.

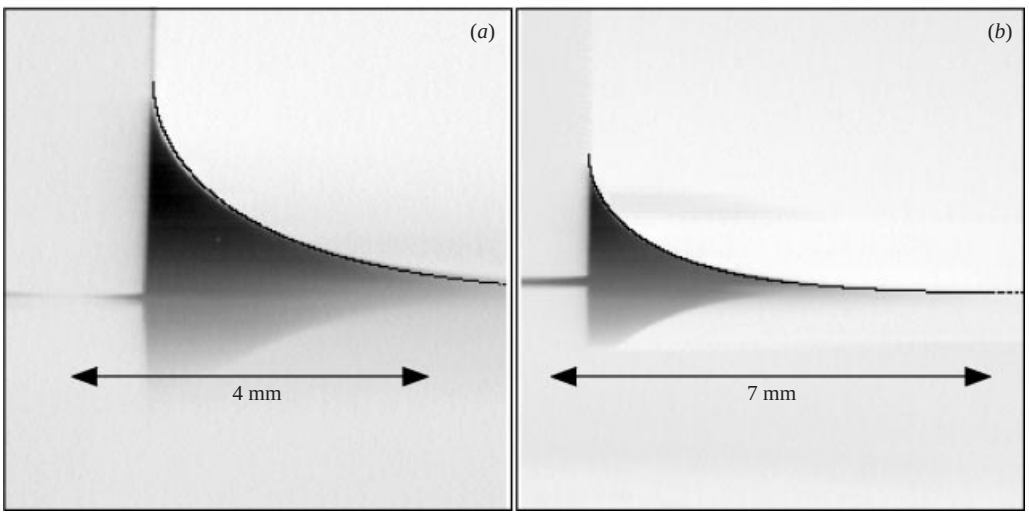

FIGURE 11. Comparison between the observed static meniscus and the theoretical shape derived from equation (4.4): (*a*) hexane with $r_0 = 8.0$ mm, (*b*) V1000 with $r_0 = 8.0$ mm.

The meniscus shape $z(r)$ results from another integration of equation (4.3) which can be written in the implicit form:

$$\frac{1}{2}\ln\left(\frac{1+\sqrt{1-(z/a)^2/4}}{1-\sqrt{1-(z/a)^2/4}}\right) - 2\sqrt{1-(z/a)^2/4} = r/a + K, \tag{4.4}$$

where K is a constant to be determined with the limit condition in $r = 0$. The corresponding shape is presented in figure 10(*a*), where equation (4.4), shown as a solid line, is completed by its symmetric part, shown as a dotted line, which expresses that the meniscus shape is the same when the liquid is at the right or at the left of the wall. In the case $\theta_e = 0$, the position of the wall is indicated in figure 10(*a*). The relation $K(\theta_e)$ is displayed in figure 10(*b*).

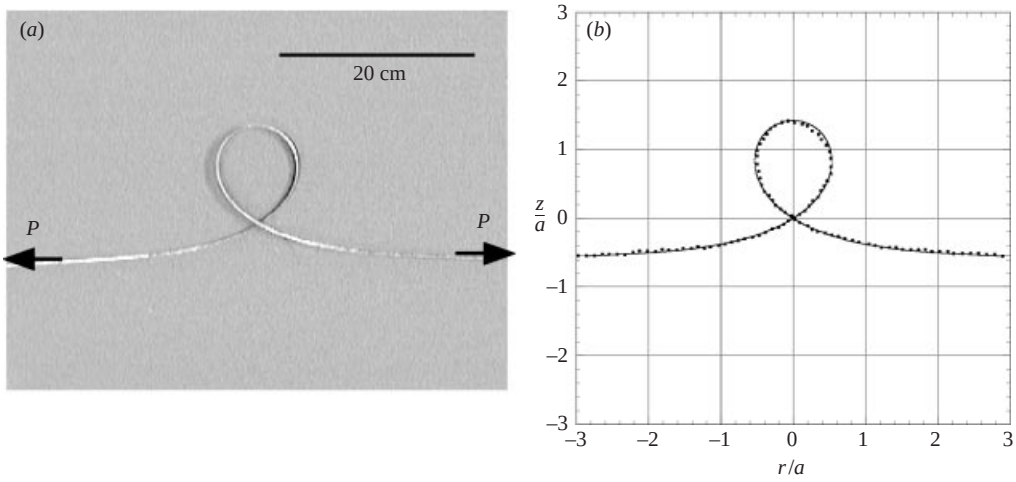

FIGURE 12. Comparison between (*a*) the observed shape of a thin sheet of stainless steel and (*b*) the theoretical shape derived from equation (4.4).

This theoretical shape is compared in figure 11 with the static meniscus observed experimentally with hexane (figure 11*a*) and V1000 (figure 11*b*) for $r_0 = 8.0\,\mathrm{mm}$.

In Maxwell (1875), it states that "The form of the capillary surface is identical with that of the elastic curve ...". This analogy has been tested using a stretched stainless steel saw blade (figure 12*a*), the shape of which is compared with the looping described by equation (4.4) in figure 12(*b*). In this experiment, the capillary length is defined by $a \equiv \sqrt{EI/P}$, where $E \approx 2 \times 10^{11}\,\mathrm{Pa}$ is the Young modulus, $I \approx 2.5 \times 10^{-13}\,\mathrm{m}^4$ the moment of inertia of the sheet, and $P \approx 10\,\mathrm{N}$ the applied stretching force. These values lead to $a \approx 7\,\mathrm{cm}$ and the non-dimensional observed loop compares satisfactorily with the curve presented in figure 10(*a*). A more detailed discussion of this analogy can be found in Roman, Gay & Clanet (2001).

4.1.3. *Meniscus on a small fibre*

The small fibre limit is defined by $r_0 \ll a$. Then, as long as r remains small compared to a, the shape of the meniscus can be obtained by neglecting gravity in equation (4.1), which yields

$$\frac{\mathrm{d}\theta}{\mathrm{d}s} = \frac{\cos\theta}{r + r_0}. \tag{4.5}$$

This equation expresses the equality of the two principle radii of curvature and leads to a catenary:

$$\frac{r_0 + r}{\cos\theta_e} = r_0 \cosh\left[\frac{z_e - z}{r_0 \cos\theta_e + \ln/((1+\sin\theta_e)/\cos\theta_e)}\right]. \tag{4.6}$$

In this algebraic expression for the shape, the meniscus height z_e is unknown and cannot be determined by the condition at r_∞ since equation (4.6) only holds in the domain $r \ll a$. However, z_e can be chosen such that the corresponding catenary has the volume of the meniscus given by equation (4.2). This argument leads to

$$z_e \approx r_0 \cos\theta_e \ln\left[\frac{4a}{r_0(1+\sin\theta_e)}\right]. \tag{4.7}$$

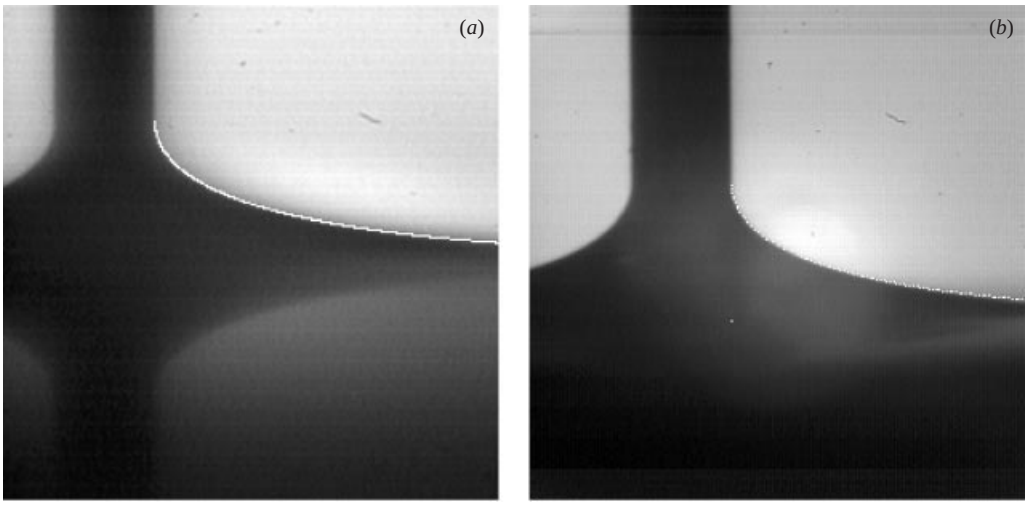

FIGURE 13. Comparison between the observed static meniscus and the theoretical shape derived from the numerical integration of equation (4.1) (continuous line in *a*), and from the asymptotic solution presented in equation (4.6) and (4.8) (dotted line in *b*): (*a*) hexane with $r_0 = 0.225$ mm, (*b*) V1000 with $r_0 = 0.225$ mm.

This approximation represents the first term of an expression derived by James (1974), through an asymptotic matching between the inner catenary solution and the outer region where gravity can no longer be neglected:

$$z_e \approx r_0 \cos\theta_e \ln\left[\frac{4a}{r_0(1+\sin\theta_e)} - \gamma\right], \tag{4.8}$$

where $\gamma \equiv 0.58$ is the Euler constant. This expression was later improved by Lo (1983) for $\theta_e \neq 0$. Figure 13 shows two static menisci observed experimentally with hexane (13*a*) and V1000 (13*b*): the shape obtained by integrating numerically equation (4.1) is drawn (full line in figure 13*a*), together with the shape given by equations (4.6) and (4.8) (dotted line in figure 13*b*). In both cases, the calculated shape is very close to the observed meniscus. This verification allows us to use James' asymptotic expression of the height for small fibres ($Bo \leqslant 1$): the relative error in the height using equation (4.8) is 20% below the actual value for $Bo = 1$, 10% for $Bo = 0.8$ and smaller than 1% for $Bo \leqslant 0.3$.

4.2. *The dynamic meniscus*

To describe the dynamics of the meniscus, we develop an integral model based on a driving capillary force F_c, acting on the meniscus of mass M, velocity U (figure 14), and subjected to a viscous force F_v.

4.2.1. *Inertial meniscus on a planar wall*

In this limit ($Ka \gg 1$, $Bo \gg 1$, domain 4), we can neglect viscous forces and balance the capillary force with both inertia and gravity:

$$\frac{\mathrm{d}(MU)}{\mathrm{d}t} = F_c - Mg. \tag{4.9}$$

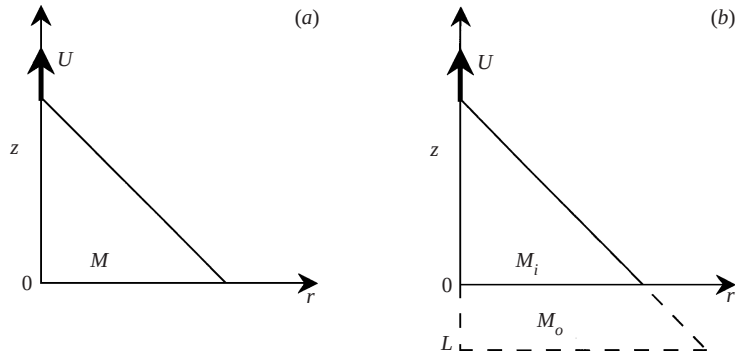

FIGURE 14. Sketch of the dynamic meniscus (*a*) with no added mass and (*b*) with an added mass.

At equilibrium, $F_c = M_e g$, where M_e is the mass of the static meniscus. From equation (4.2), $M_e = 2\pi\rho r_0 a^2$, and we deduce $F_c = 2\pi r_0 \sigma$. Equation (4.9) can then be written

$$\frac{\mathrm{d}(MU)}{\mathrm{d}t} = F_c \left(1 - \frac{M}{M_e}\right), \tag{4.10}$$

where the ratio of mass M/M_e is of order $(z/a)^2$. In the limit $z/a \ll 1$, the right-hand side of equation (4.10) reduces to F_c. The observation of the meniscus during the rise (figures 4, 7 and 8*b*) suggests that the meniscus shape can be approximated by a corner $r = \alpha z$, so that $M \approx \alpha\pi\rho r_0 z^2$. Then, equation (4.10) reduces to

$$\frac{\mathrm{d}^2 z^3}{\mathrm{d}t^2} \approx \frac{6}{\alpha}\frac{\sigma}{\rho}. \tag{4.11}$$

Equation (4.11) can be integrated twice with the initial condition $z(t = 0) = 0$ which leads to

$$z \approx (3/\alpha)^{1/3} \left(\frac{\sigma t^2}{\rho}\right)^{1/3}. \tag{4.12}$$

We find here the scaling of all capillaro-inertia phenomena with no characteristic length scale ($z^3 \sim \sigma t^2/\rho$), first proposed by Keller & Miksis (1983). Note that this differs from the inertial capillary rise in a tube (Quéré 1997), where the mass is simply proportional to z, so that a constant rising velocity is found for the meniscus, $z \sim t$.

The measured height z for hexane rising along large rods is presented in figure 15 versus $\sigma t^2/\rho$. In the range $z < 0.7 z_e$, the slope is found to be 0.34 ± 0.01, and the best fitting linear relation in $t^{1/3}$ yields $z = 0.65(\sigma t^2/\rho)^{1/3}$. This function is the straight line in figure 15. The 1/3 power law is achieved up to $z/z_e \approx 0.7$. Since the static meniscus height varies as $z_e = \sqrt{2}a$, a characteristic time for the rise should be $t_e \approx 3.2\sqrt{\rho a^3/\sigma}$.

Concerning the prefactor 0.65 for the contact line trajectory, we find from equation (4.12) that this corresponds to $\alpha \approx 10$. This discrepancy with the value observed in figure 8(*b*) ($\alpha \approx 1.4$) can be understood qualitatively by taking into account the entrained mass in the bath: for the remaining part of the liquid, the dynamic meniscus acts as a sink. Over a characteristic distance of order z, the fluid under the meniscus is set into motion with a characteristic speed $\dot{z}$. To correct the model and account for this entrained added mass, we assume that our system is composed of an internal mass M_i plus an outside mass M_o characterized by a length $L = \beta z$ (see figure 14*b*).

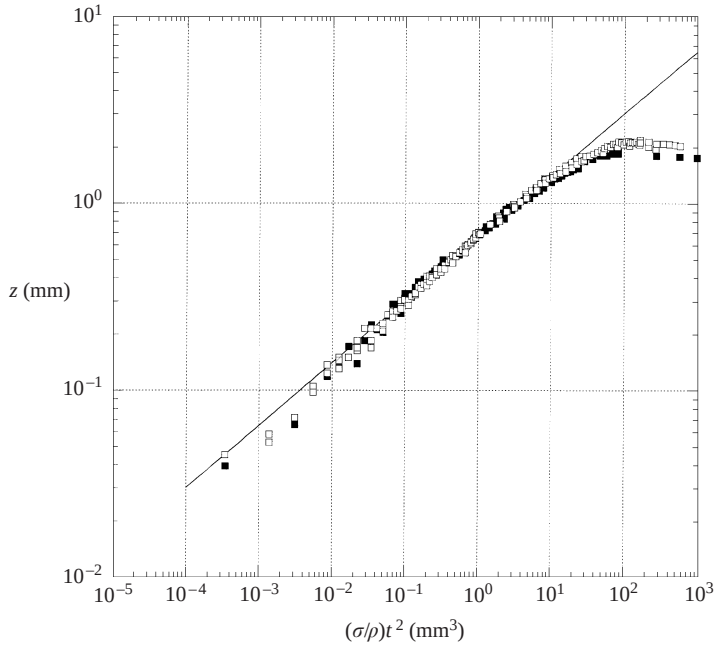

FIGURE 15. Dynamic of the meniscus obtained with hexane: ■, $r_0 = 8$ mm; □, $r_0 = 4$ mm. The straight line corresponds to the linear relationship $z = 0.65(\sigma t^2/\rho)^{1/3}$.

These assumptions modify the equation of motion to

$$\frac{\mathrm{d}}{\mathrm{d}t}\left[(M_i + M_o)U\right] = F_c - M_i g, \tag{4.13}$$

which can be integrated through similar steps and leads to a corrected expression for the contact line trajectory:

$$z \approx \left(\frac{3}{\alpha(1+\beta)^2}\right)^{1/3}\left(\frac{\sigma t^2}{\rho}\right)^{1/3}. \tag{4.14}$$

With $\alpha \approx 1.4$, we find from the experimental prefactor 0.65, that β lies between 1.5 and 2. The entrained mass is thus far from negligible in this problem, a difference, again, with the capillary rise problem, where the entrainment effect develops on a length of order r_0, the radius of the tube (Szekeley, Neumann & Chuang 1971).

4.2.2. *Inertial rise on a small fibre*

In this limit ($Ka \gg 1$, $Bo \ll 1$, domain 3), the meniscus is an axisymmetrical cone, which modifies the way the mass scales with z:

$$M \approx \frac{\pi}{3}\alpha^2 \rho z^3. \tag{4.15}$$

Considering again the beginning of the rise, $z \ll (r_0 a^2)^{1/3}$, the equation of motion (4.13) is written

$$\frac{\mathrm{d}^2 z^4}{\mathrm{d}t^2} = \frac{24}{\alpha^2}\frac{\sigma r_0}{\rho}. \tag{4.16}$$

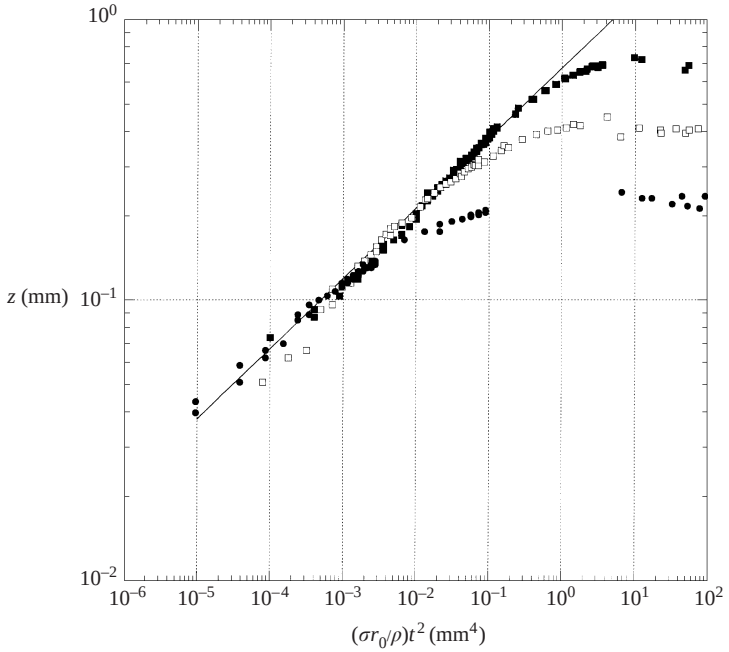

FIGURE 16. Dynamic of the meniscus obtained with hexane: ●, $r_0 = 0.0625$ mm; □, $r_0 = 0.13$ mm; ■, $r_0 = 0.26$ mm. The straight line corresponds to the best fit linear relationship $z = 0.67(\sigma r_0 t^2/\rho)^{1/4}$.

Equation (4.16) can be integrated twice with the initial condition, $z(t = 0) = 0$, which leads to

$$z \approx (12/\alpha^2)^{1/4} \left(\frac{\sigma r_0 t^2}{\rho}\right)^{1/4}. \tag{4.17}$$

The height z observed experimentally with hexane and small fibres is presented in figure 16 versus $\sigma r_0 t^2/\rho$, together with the best fit linear relationship. One observes in this figure that the three trajectories reach different equilibrium heights, as shown in § 4.1.3. But the first part of the rise collapses on a single curve, approximated well by $z = 0.67(\sigma r_0 t^2/\rho)^{1/4}$. Since $z_e \sim r_0$, one deduces that the characteristic time of establishment of the meniscus is $t_e \approx 2.2\sqrt{\rho r_0^3/\sigma}$. The prefactor 0.67 in the contact line trajectory again implies a value of β standing between 1.5 and 2, characterizing the entrained mass.

4.2.3. *Viscous rise on a planar wall*

The viscous regime is very different, as observed in figure 7, where the meniscus is found to be quasi-static, for each dynamic contact angle θ. Thus, for menisci satisfying $Ka \ll 1$ and $Bo \gg 1$ (domain 1), we expect equation (4.3) to be obeyed. This can be tested easily by plotting, as in figure 17, the observed $\sin\theta$ as a function of the measured quantity $1 - \frac{1}{2}(z/a)^2$. A linear relation is indeed found, confirming that the shape of the meniscus is quasi-static during its onset.

The capillary force $F_c = 2\pi r_0 \sigma$ can be written

$$\frac{F_c}{2\pi r_0} = \sigma\cos\theta + \sigma(1 - \cos\theta). \tag{4.18}$$

The first term in the right-hand side of equation (4.18) is balanced by the weight of

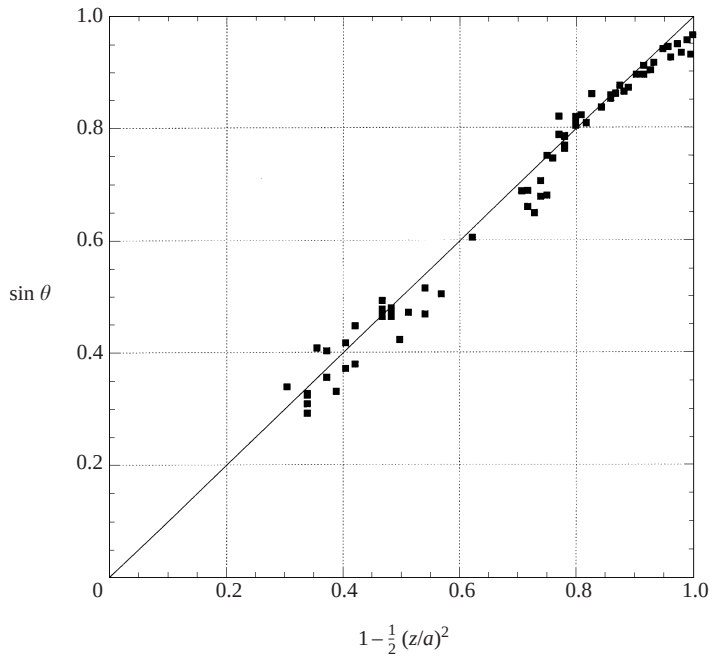

FIGURE 17. Comparison between the sine of the observed angle and the sine of the calculated angle from the quasi-steady approach, $\sin\theta = 1 - 1/2(z/a)^2$. The continuous line represents an equality between both terms.

the meniscus and is responsible of the quasi-steady shape observed. The second term, $\sigma(1-\cos\theta)$, is responsible for the motion of the contact line. Balancing this force with the viscous one close to the moving edge leads to Tanner's law, which relates the dynamical contact angle with the line velocity: $\theta^3 = C_1\eta U/\sigma$, where $C_1 \approx 80$ is a constant. This law, established experimentally by Hoffman (1975) and Tanner (1979) and derived theoretically for small θ by Cox (1986) and Gennes (1985), surprisingly turns out to be valid up to $\theta \approx 150°$. Together with equation (4.3), Tanner's law leads to an evolution equation for the contact angle:

$$\frac{\mathrm{d}\theta}{\mathrm{d}t} = -\frac{\theta^3\sqrt{1-\sin\theta}}{\cos\theta}, \tag{4.19}$$

where the time is scaled by $\tau = (C_1/\sqrt{2})\eta a/\sigma$. At short times, $\theta(t) \approx \pi/2 - \epsilon(t)$, equation (4.19) leads to the linear evolution: $\theta(t) \approx \pi/2 - \pi^3 t/8\sqrt{2}$. At long times, where $\theta \ll 1$, a linearization of equation (4.19) yields a slow relaxation for the contact angle: $\theta \sim 1/\sqrt{t}$. For the whole trajectory, equation (4.19) can be integrated with the initial condition $\theta(t=0) = \pi/2$. The law $\theta(t)$ is then used to determine the contact line location $z(t)$ using equation (4.3): $z(t) = \sqrt{2(1-\sin\theta(t))}a$. This integrated trajectory is compared in figure 18 with the behaviours observed with V1000 and large fibres. Without any adjustable parameter, the comparison is satisfactory until equilibrium.

For the asymptotic behaviours of the trajectory, one finds that $z/a \sim t/\tau$ at small time ($t \ll \tau$) and that $z/a \sim \sqrt{1-1/\sqrt{t/\tau}}$ when approaching equilibrium ($t \gg \tau$). It must be stressed that the linear asymptotic behaviour can only be observed at very small times, i.e. for $t/\tau < 10^{-3}$. In the time range in which the experiments are conducted, we essentially observe matching between the linear regime and the static behaviour.

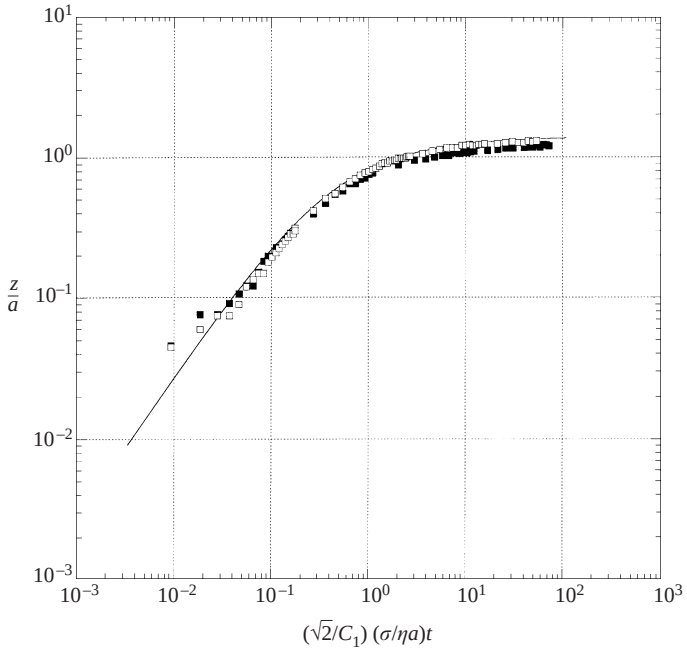

FIGURE 18. Comparison between the integration of equation (4.19) (continuous line) and the viscous meniscus trajectories observed with V1000: ■, $r_0 = 8\,\text{mm}$; □, $r_0 = 4\,\text{mm}$.

4.2.4. *Viscous rise on a small fibre*

In this limit ($Ka \ll 1$, $Bo \ll 1$, domain 2), we neglect inertia and follow the same approach as for domain 1. We assume a quasi-steady meniscus, with a height now given by equation (4.8). Using Tanner's law, the time evolution of the apparent contact angle is then described by the differential equation

$$\frac{\mathrm{d}\theta}{\mathrm{d}t} = -\frac{\theta^3}{f(\theta, Bo)}, \tag{4.20}$$

where

$$f(\theta, Bo) = \sin\theta \left[\ln\left(\frac{4}{Bo(1+\sin\theta)}\right) - \gamma\right] + \frac{\cos^2\theta}{1+\sin\theta}. \tag{4.21}$$

The characteristic time used to scale equation (4.20) is $\tau = C_1\eta r_0/\sigma$. At short times, ($t \ll \tau$), $\theta \approx \pi/2 - \dot{\theta}_0 t$, with $\dot{\theta}_0 = (\pi/2)^3/(\ln 2/Bo - \gamma)$. At long times, $f(\theta, Bo) \approx 1$ and we recover the behaviour observed with large fibres $\theta \sim 1/\sqrt{t}$. More quantitatively, equation (4.20) can be integrated with the initial condition $\theta(t=0) = \pi/2$. The $\theta(t)$ relation is then used in equation (4.8) to obtain the contact line trajectory $z(t)$. The comparison between the integrated trajectory and the one observed experimentally with V1000 and different Bond numbers is presented in figure 19 (□, $Bo = 0.15$ and ■, $Bo = 0.087$). Again, without any adjustable parameter, this comparison reveals a satisfactory agreement up to equilibrium.

5. Conclusion

We have studied experimentally the time evolution of a wetting liquid interface along a vertical cylindrical fibre, from the contact to the steady meniscus. Con-

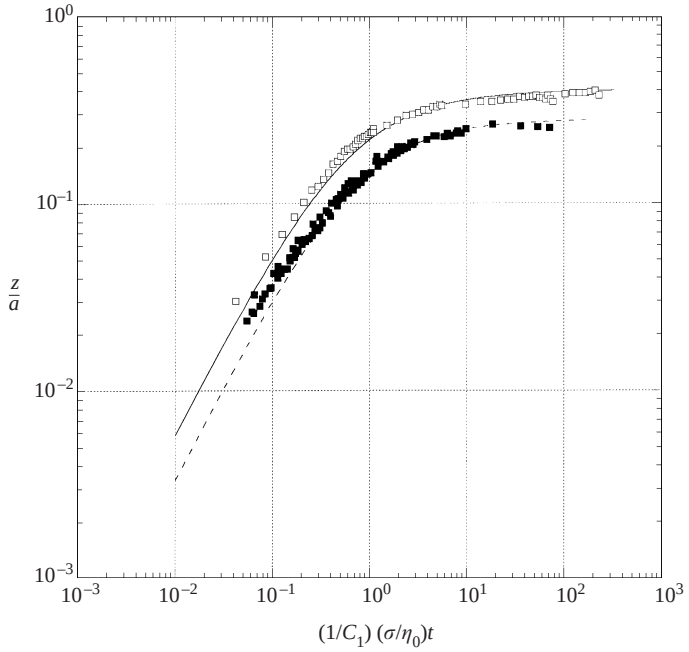

FIGURE 19. Comparison between the integration of equation (4.20) (continuous and dashed line) and the viscous meniscus trajectories observed with V1000: ■, $r_0 = 0.13$ mm; □, $r_0 = 0.225$ mm.

sidering viscous and non-viscous liquids forming menisci on large rods and small fibres, we have defined four domains, characterized by different dynamics and scaling parameters.

For non-viscous liquids on a large rod, we have shown that the meniscus height z increases as $(\sigma/\rho)^{1/3}t^{2/3}$. Thus, the static position ($z \sim a$) is reached after a characteristic time $t_e \sim \sqrt{\rho a^3/\sigma}$. For water, $t_e \approx 10$ ms.

For non-viscous liquids that rise on a small fibre, the scaling for the height is modified for geometric reasons: the height z is found to scale as $(\sigma r_0/\rho)^{1/4}t^{1/2}$. Then, the static meniscus ($z \sim r_0$) is reached after $t_e \sim \sqrt{\rho r_0^3/\sigma}$, which varies quickly with r_0 (for $r_0 \approx 10\,\mu$m, we find $t_e \approx 10\,\mu$s with water).

The dynamics of viscous liquid rising on large or small fibres is described well by a quasi-static model, based on a steady meniscus shape and on Tanner's law. For large fibres, the length scale is a, and the time scale $80\eta a/\sigma$. With an oil 1000 times more viscous than water, we find $t_e \approx 8$ s. For small fibres, the length scale is r_0 and the time scale $80\eta r_0/\sigma$. With the same oil on a 10 μm fibre, we find $t_e \approx 40$ ms.

We thank the referees for their valuable comments and suggestions as well as J. Magnaudet and H. A. Stone for discussions on the Kapitsa–Morton number.

REFERENCES

BOUASSE, H. 1924 *Capillarité, Phénomènes Superficiels*. Librairie Delagrave, Paris.

COX, R. G. 1986 The dynamics of the spreading of a liquid on a solid surface. *J. Fluid Mech.* **168**, 169–189.

FULFORD, G. D. 1964 The flow of liquids in thin films. *Adv. Chem. Engng* **5**, 151–236.

de Gennes, P. G. 1985 Wetting: statics and dynamics. *Rev. Mod. Phys.* **57**, 827–863.

Haberman, W. L. & Morton, R. K. 1954 An experimental study of bubbles moving in liquids. *Trans. ASCE* **387**, 227–252.

Hauksbee, F. 1709 *Physico-Mechanical Experiments*, pp. 139–169. London.

Hoffman, R. L. 1975 A study of the advancing interface. *J. Colloid Interface Sci.* **50**, 228–241.

James, D. F. 1974 The meniscus on the outside of a small circular cylinder. *J. Fluid Mech.* **63**, 657–664.

Kapitsa, P. L. 1948 Wave flow of thin layers of a viscous fluid. *Zh. Eksperim. i Teor. Fiz.* **18**, 3 (in Russian).

Keller, J. B. & Miksis, M. J. 1983 Surface tension driven flows. *SIAM J. Appl. Maths* **43**, 268–277.

Landau, L. & Lifchitz, E. 1971 *Physique Theorique: Mecanique des Fluides.* Editions Mir.

Laplace, P.-S. 1806 *Mecanique Celeste.*

Lo, L. L. 1983 The meniscus on a needle – a lesson in matching. *J. Fluid Mech.* **132**, 65–78.

Maxwell, J. C. 1875 Capillary action. In *Encyclopaedia Britannica*, 9th Edn.

E. Pitts, E. 1976 The stability of a meniscus joining a vertical rod to a bath of liquid. *J. Fluid Mech.* **76**, 641–651.

Quéré, D. & di Meglio, J. M. 1994 The meniscus on a fibre. *Adv. Colloid Interface Sci.* **48**, 141–150.

Quéré, D. 1997 Inertial capillarity. *Europhys. Lett.* **39**, 533–538.

Roman, B., Gay, C. & Clanet, C. 2001 Pendulum, drops and rods, a physical analogy. *Am. J. Phys.* (submitted).

Szekeley, J., Neumann, A. W. & Chuang, Y. K. 1979 The rate of capillary penetration and the applicability of the Washburn equation *J. Colloid Interface Sci.* **35**, 273–278.

Tanner, L. 1979 The spreading of silicone oil drops on horizontal surfaces. *J. Phys.* D: *Appl. Phys.* **12**, 1473–1484.

Washburn, E. W. 1921 The dynamics of capillary flow. *Phys. Rev.* **17**, 273–283.

White, D. A. & Tallmadge, J. A. 1965 Static menisci on the outside of cylinders. *J. Fluid Mech.* **23**, 325–335.